RSC Advances

ROYAL SOCIETY OF CHEMISTRY

www.rsc.org/advances

Cite this: DOI: 10.1039/c0xx00000x

www.rsc.org/xxxxxx

ARTICLE TYPE

Template-free synthesis of mesoporous CeO_2 powders by integrating bottom-up and top-down routes for acid orange 7 adsorption

Yaohui Xu[a] and Ruixing Li*[a]

Received (in XXX, XXX) Xth XXXXXXXXX 20XX, Accepted Xth XXXXXXXXX 20XX

DOI: 10.1039/b000000x

A combined bottom-up and top-down route was developed for the template-free synthesis of mesoporous CeO_2 powders using $Ce(NO_3)_3{\cdot}6H_2O$, NH_4HCO_3, H_2O_2, and H_2O as starting reagents. The flake-like $Ce_2(CO_3)_3{\cdot}8H_2O$ precursor was etched by H_2O_2, and CeO_2 nucleated *in situ* with built-in equiaxed particles. Pores formed on the flakes owing to the loss of by-products of H_2O and CO_2. The formation of the mesostructured CeO_2 could also be explained by the large change in volume induced as a result of the difference in density between $Ce_2(CO_3)_3{\cdot}8H_2O$ and CeO_2. Accordingly, the original flake-like morphology of $Ce_2(CO_3)_3{\cdot}8H_2O$ was not preserved upon pore formation and during continuous stirring in the synthesis. Subsequent hydrothermal treatment destroyed the loose aggregates of CeO_2 derived from the reaction between H_2O_2 and $Ce_2(CO_3)_3{\cdot}8H_2O$. Rearrangement of the CeO_2 particles *via* dissolution–recrystallization process occurred under certain temperatures and pressures. Consequently, CeO_2 particles with coarser sizes, smoother surfaces, and mesoporous structures were obtained. The specific surface area of the particles was 166.5 m^2/g after hydrothermal treatment at 200 °C for 24 h. The mesoporous CeO_2 particles possessed better adsorption capacities of acid orange 7 dye than basic orange 2 dye in the absence of pH pre-adjustments. The saturated adsorption amount of acid orange 7 dye was 510.2 mg/g at 298 K based on Langmuir linear fitting of the experimental data.

Introduction

Ceria (CeO_2) nanostructures have been widely used because of their unique crystal structure and redox property,[1,2] such as in solid oxide fuel cells,[3] oxygen storage capacitors,[4,5] dye removal treaments,[6,7] and as catalysts,[8] ultraviolet blocking materials,[9,10] chemical mechanical polishing materials,[11] and oxygen ion conductivity materials.[12] The performances of CeO_2 can be tailored by controlling its structure and synthesis processes.

Integration of bottom-up and top-down routes has recently become one of the dominant challenges in the fabrication of nano-/micro-structures/devices with advanced functional properties.[13–19] The preparation of mesoporous CeO_2 is typically based on a bottom-up approach; however, it also requires a combination of top-down processes. In top-down processes, the removal of the structure-directing agents or the calcination of the cerium precursors is usually involved. For example, Ni *et al.* synthesized mesoporous CeO_2 particles *via* a sol–gel method using Pluronic P123 or F127 *tri*-block copolymer as a surfactant, and the surfactant was removed by calcination.[20] In another study, Zhang *et al.* synthesized mesoporous CeO_2 nanotube arrays using as-prepared ZnO nanorod arrays as templates. The templates were successively submerged in the NaOH solution, deionized water, and $Ce(NO_3)_3$ solution. Following annealing at 500 °C for 30 min, the mesoporous polycrystalline CeO_2 nanoshells on ZnO were obtained. Finally, mesoporous CeO_2 nanotube arrays were obtained by dissolving ZnO using HNO_3.[21] Nabih *et al.* demonstrated an inverse mini-emulsion technique to synthesize mesoporous CeO_2 nanoparticles. Cetyltrimethylammonium bromide or poly(ethylene oxide)-b-poly(propylene oxide)-b-poly(ethylene oxide) *tri*-block copolymers as a template, was incorporated into mini-emulsion droplets. The solvent was removed by freeze-drying and mesoporous CeO_2 was obtained by following calcination at 400 °C.[22] Though template-assisted approaches are efficient in fabricating mesoporous CeO_2 nanostructures, tedious procedures are required for the separation of the CeO_2 mesoporous structures. To date, only a few studies on direct and template-free synthesis of mesoporous CeO_2 have been reported.[23,24]

Acid orange 7 (AO7) is one of the most common azo dyes employed in various industries ranging from textile to paper.[25] Likewise to most azo dyes, it is difficult to biologically degrade AO7 because of the strong azo bond, –N=N–. AO7 dye may accumulate in the environment under the reaction of microorganisms and may generate carcinogenic and mutagenic effects to human and aquatic organisms.[26,27] To date, numerous approaches have been employed to remove AO7 dye from aqueous solution, such as electrochemical techniques,[28] bio-degradation processes,[29] photocatalytic oxidations,[30] and adsorptive removal processes using diverse adsorbents[31]. Among the available chemical and physical processes, adsorption using adsorbents is the most versatile and widely used technique.[32,33]

In this work, we developed an combined of bottom-up and top-down route for the template-free synthesis of mesoporous CeO_2

powders. The possible mechanisms for the transformation from $Ce_2(CO_3)_3{\cdot}8H_2O$ into CeO_2 and morphology evolution from flake-like to mesoporous structures were discussed. Additionally, the absorption characteristics of the mesoporous CeO_2 particles for AO7 were investigated. As a comparison, the adsorption capacity of anther azo dye, basic orange 2 (BO2), was also determined.

Experimental

Materials

$Ce(NO_3)_3{\cdot}6H_2O$ (99.95 %), NH_4HCO_3 (ACS), and AO7 dye were supplied by Aladdin Co. Ltd. BO2 dye was obtained from China National Chemical Corporation. H_2O_2 (30 %) was purchased from Beijing Chemical Works. All major chemicals were used as received without further purification. Distilled water was used in all experiments.

Synthesis of mesoporous CeO_2 particles

A flow chart of the synthesis procedure employed is shown in Fig. 1. Typically, 1.737 g $Ce(NO_3)_3{\cdot}6H_2O$ was dissolved in 28 mL distilled water under vigorous stirring until a clear Ce^{3+} solution was formed. Then, stoichiometrically excess 1.265 g NH_4HCO_3 was added to the Ce^{3+} solution under continuous stirring; a white precipitate (labeled as Precursor) was generated immediately. Subsequently, the white suspension promptly turned orange after dropwise addition of 7 mL H_2O_2, The suspension was stirred for 30 min (Precursor 21) and aged for 3 h (Precursor 22). Excess stoichiometric amounts of NH_4HCO_3 and H_2O_2 were used. Precursor 22 in the total mother liquor was carefully decanted into a 50 mL Teflon-lined stainless steel autoclave, which was heated at 200 °C for 24 h to give Sample 2. Additionally, Sample 1 was synthesized hydrothermally under the same conditions, however, in the absence of H_2O_2. All the obtained products were washed and dried under vacuum at 60 °C for 24 h.

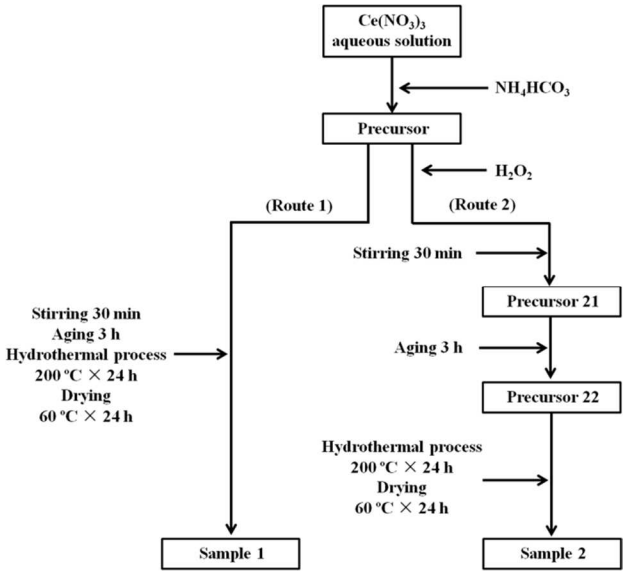

Fig. 1. Samples synthesized using two routes *i.e.*, in the absence (Route 1) and presence (Route 2) of H_2O_2.

Characterization

The crystallographic phases of the samples were characterized by X-ray diffraction (XRD) using graphite monochromatized Cu Kα radiation (Rigaku, D/MAX 2200 PC). The morphologies of the samples were evaluated by field-emission scanning electron microscopy (SEM; JEOL-7500F) and transmission electron microscopy (TEM; JEOL JEM-2100F). Nitrogen adsorption–desorption isotherms were measured on a QuadraSorb SI. The infrared measurements were employed by a Fourier transform infrared spectrometer (FT-IR; Nicolet 6700).

Adsorption studies

The adsorption characteristics of the mesoporous CeO_2 powders were evaluated by adsorptive removal of AO7 and BO2 dyes from simulated wastewater in the dark. The adsorption studies were conducted without pH pre-adjustments in the dark, as a function of initial dye concentration (20−100 mg/L), contact time (0–60 min) and adsorbent dosage (2.0 g/L) at constant temperature (298 K) and agitation speed (200 rpm). Typically, 0.2 g synthesized sample was dispersed into 100 mL of AO7 solution at varying concentrations (20, 40, 60, 80, and 100 mg/L). The mixture was stirred at a constant temperature. Then, suspension aliquots of ~4 mL were withdrawn at regular intervals and centrifuged (8000 rpm). The absorbance of the supernatant was measured at the maximum absorption wavelength (484 nm for AO7, and 452 nm for BO2) using an ultraviolet–visible spectrophotometer (Techcomp UV-2600). The adsorption efficiency (η, %) of AO7 was calculated using Eq. 1, and the adsorption amount (q, mg/g) was calculated using Eq. 2:[34]

$$\eta = \frac{C_0 - C_e}{C_0} \times 100\ \% \quad (1)$$

$$q = \frac{(C_0 - C_e)V}{m} \quad (2)$$

where C_0 (mg/L) is the initial concentration of dye, C_e (mg/L) is the concentration of the dye (adsorbate) at equilibrium, m (g) is the mass of the absorbent (CeO_2), and V (L) is the volume of the aqueous solution.

The Langmuir model (Eq. 3) was used to examine the adsorption characteristics:[35]

$$q = \frac{K_L q_m C_e}{1 + K_L C_e} \quad (3)$$

where q_m (mg/g) is the saturated adsorption amount of dye adsorbed *per* unit weight of adsorbent and K_L (L/mg) is the Langmuir constant related to the affinity of binding sites. Equation 3 can be rearranged to a linear form (Eq. 4).[36] Hence, the values of q_m and K_L can be respectively evaluated according to the slope and intercept of the straight line of the plot of (C_e/q) *vs*. C_e.

$$\frac{C_e}{q} = \frac{1}{K_L q_m} + \frac{C_e}{q_m} \quad (4)$$

Results and discussion

Synthesis and characterization

The crystallographic phases of the samples were determined by XRD. Figure 2 shows the XRD patterns of the precursors and obtained samples. More specifically, Fig. 2a shows the XRD pattern of the original precipitate (Precursor) after adding

NH_4HCO_3 to Ce^{3+} solution, The two diffraction peaks centered at 10.8 ° and 21.4 ° were assigned to $Ce_2(CO_3)_3{\cdot}8H_2O$ (JCPDS No. 38-0377; density = 2.790 g/cm^3). The XRD pattern was similar to that obtained in a previous study for $Ce_2(CO_3)_3{\cdot}8H_2O$.[37] This sample was further characterized by FT-IR analysis. As observed in Fig. S1 (ESI,†), the FTIR spectrum was also consistent with that obtained for cerous carbonate hydrate;[38] the presence of the CO_3^{2-} group was confirmed by the peaks observed at ~1488 and 1424 cm^{-1}. Figure 2b, c shows the XRD patterns of the products obtained following addition of H_2O_2 and subsequent stirring for 30 min and aging for 3 h (Precursor 21 and Precursor 22, respectively). As observed, the peaks related to $Ce_2(CO_3)_3{\cdot}8H_2O$ were no longer present that suggested the reduced crystallinity of the samples. Further analysis of the phase structures was conducted by selected area electron diffraction (SAED) analysis as discussed later. Figure 2d shows the XRD pattern of the product obtained after hydrothermal treatment at 200 °C for 24 h (Sample 2). The pattern displayed several well-resolved peaks that could be indexed to the (111), (200), (220), and (331) planes of face-centered cubic CeO_2 (JCPDS No. 34-0394; density = 7.215 g/cm^3). The mean crystallite size of Sample 2 was ~4.6 nm, as calculated by Scherrer formula. In contrast, the XRD pattern of Sample 1 (prepared in the absence H_2O_2) in Fig. 2e displayed a mixture of CeO_2 and $Ce(CO_3)OH$ characteristic peaks (JCPDS No. 52-0352).

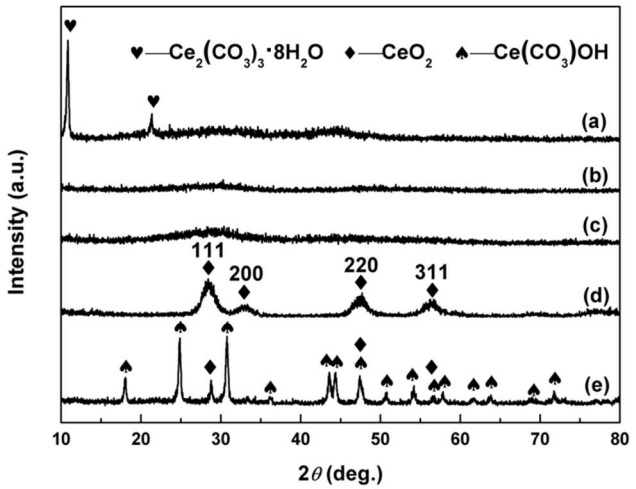

Fig. 2. XRD patterns of the products obtained following (a) addition of NH_4HCO_3 to the Ce^{3+} solution (Precursor), (b) addition of H_2O_2 and subsequent stirring for 30 min (Precursor 21), (c) aging for 3 h (Precursor 22), (d) hydrothermal treatment at 200 °C for 24 h (Sample 2), and (e) hydrothermally treatment (without addition of H_2O_2) (Sample 1).

The morphologies of the samples are shown in Fig. 3. As observed in Fig. 3a, $Ce_2(CO_3)_3{\cdot}8H_2O$ precursor featured a flake-like morphology. Following addition of H_2O_2, the flakes were mostly substituted by numerous equiaxed particles. Closer analysis revealed that the flakes comprised built-in equiaxed particles (Fig. 3b). This finding suggested the possible *in situ* evolution of small CeO_2 particles in the carbonate precursor framework and formation of debris by continuous stirring during addition of H_2O_2. After aging for 3 h, flakes were no longer present and the equiaxed particles formed loose agglomerates (Fig. 3c). A completely different morphology was observed following hydrothermal treatment at 200 °C for 24 h. The particles grew bigger and featured smoother surfaces (Fig. 3d). In contrast, the flake-like morphology was mostly maintained in Sample 1 that was prepared in the absence of H_2O_2 (ESI,† Figure S2).

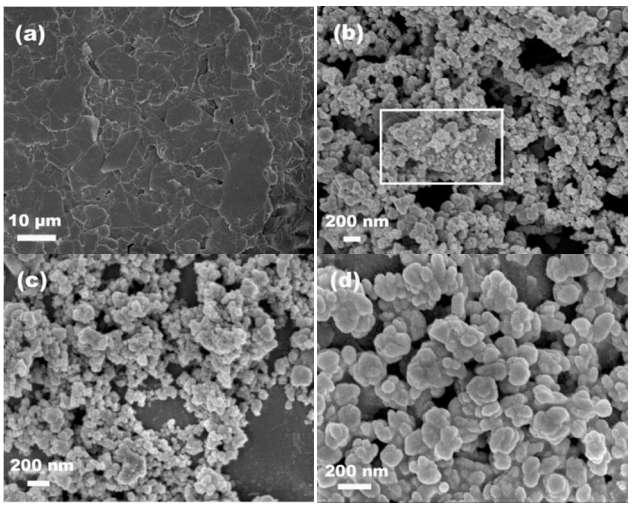

Fig. 3. SEM images of the products obtained following (a) addition of NH_4HCO_3 to the Ce^{3+} solution (Precursor), (b) addition of H_2O_2 and subsequent stirring for 30 min (Precursor 21), (c) aging for 3 h (Precursor 22), and (d) hydrothermal treatment at 200 °C for 24 h (Sample 2).

To understand the amorphous phases detected in Fig. 2b, c and the microstructures of the samples, TEM and SAED analyses were performed. As observed in Fig. 4a, the $Ce_2(CO_3)_3{\cdot}8H_2O$ flakes were dense and undulated. The SAED pattern of Precursor in Fig. 4b displayed both halo and multi-ring features, indicative of relatively low crystallinity, could be indexed to the (111), (220), and (311) planes of CeO_2. After aging for 3 h, a more typical CeO_2 multi-ring SAED pattern was obtained in Fig. 4c. Taking into account the XRD and SAED analyses, we deduced that both Precursor 21 and Precursor 22 could be identified as CeO_2 with poor crystallinity and no $Ce_2(CO_3)_3{\cdot}8H_2O$-related features. In contrast, after hydrothermal treatment, the CeO_2 particles displayed polycrystalline features (inset in Fig. 4d). Figure 4d revealed the mesoporous structure of the CeO_2 particles and presence of pores around the grains. The calculated grain size was ~5.0 nm (Fig. 4d), as consistent with the XRD analysis.

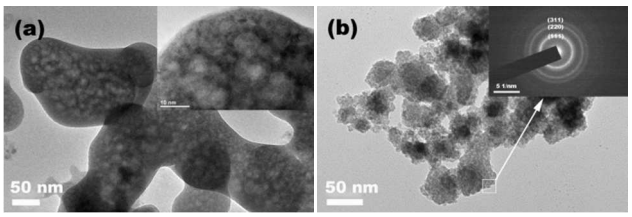

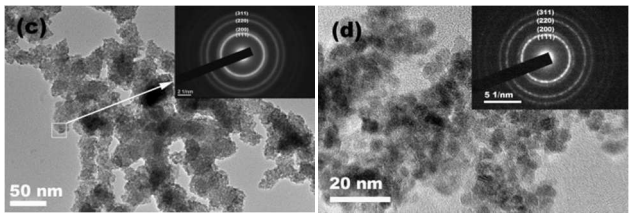

Fig. 4. TEM images of the products obtained following (a) addition of NH_4HCO_3 to the Ce^{3+} solution (Precursor), (b) addition of H_2O_2 and subsequent stirring for 30 min (Precursor 21), (c) aging for 3 h (Precursor 22), and (d) hydrothermal treatment at 200 °C for 24 h (Sample 2). (The inset in Fig. 4a shows a high-magnification HRTEM image and the insets in Fig. 4b–d show the corresponding SAED patterns.)

To further clarify the mesoporous structure of the final product CeO_2, nitrogen sorption experiments were conducted to determine its specific surface area, average pore size, and pore volume. Figure 5 shows the nitrogen adsorption–desorption isotherm of Sample 2. A hysteresis loop in the relative pressure range of 0.4–1.0 was observed, which suggested that CeO_2 was a mesoporous material.[39] Furthermore, the profile of the isotherm corresponded to that of mesoporous CeO_2 reported in the literature.[40] The specific surface area of Sample 2 was determined as 166.5 m^2/g using the Brunauer–Emmett–Teller method. The average pore size and pore volume were 3.4 nm and 0.26 cm^3/g, respectively, determined by Barrett–Joyner–Halenda analysis.

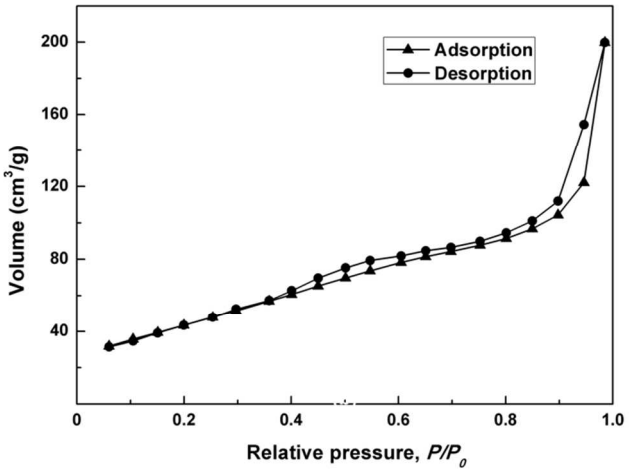

Fig. 5. Nitrogen adsorption–desorption isotherm of the hydrothermally produced mesoporous CeO_2 (Sample 2).

In summary, multidisciplinary knowledge is required to understand the products generated and processes involved in the formation of mesoporous CeO_2 from cerium nitrate hexahydrate. From a chemical perspective, the possible reactions are summarized as Reactions 1−6. The equilibria of NH_4HCO_3 in aqueous are shown in Reactions 1–4.[41] $Ce_2(CO_3)_3{\cdot}8H_2O$ is obtained upon addition of NH_4HCO_3 to Ce^{3+} solution (Reaction 5). After dropwise addition of H_2O_2, $Ce_2(CO_3)_3{\cdot}8H_2O$ is oxidized and CeO_2 is formed. At the same time, H_2O and CO_2 are produced (Reaction 6). These processes were supported by the SEM analysis in Fig. 3b, XRD and SAED analyses in Figs. 2 and 4, respectively.

$$NH_3\uparrow + CO_2\uparrow + H_2O \rightleftharpoons NH_4HCO_3 \rightleftharpoons NH_4^+ + HCO_3^- \quad (1)$$

$$NH_4^+ + OH^- \rightleftharpoons NH_4OH \rightleftharpoons NH_3\uparrow + H_2O \quad (2)$$

$$2HCO_3^- \rightleftharpoons CO_3^{2-} + CO_2\uparrow + H_2O \quad (3)$$

$$HCO_3^- + H_2O \rightleftharpoons OH^- + H_2CO_3 \quad (4)$$

$$2Ce^{3+} + 6HCO_3^- + 5H_2O = Ce_2(CO_3)_3\cdot 8H_2O\downarrow + 3CO_2\uparrow \quad (5)$$

$$Ce_2(CO_3)_3\cdot 8H_2O + H_2O_2 = 2CeO_2 + 3CO_2\uparrow + 5H_2O \quad (6)$$

Based on both theoretical and experimental results, a possible formation mechanism of the mesoporous CeO_2 particles is illustrated in Fig. 6. At the early stage of the synthesis, the flake-like $Ce_2(CO_3)_3{\cdot}8H_2O$ precursor was generated when NH_4HCO_3 was added to the Ce^{3+} solution. Etching of $Ce_2(CO_3)_3{\cdot}8H_2O$ flake with H_2O_2 generated CeO_2 *in situ* with built-in equiaxed particles (as indicated by the white box in Fig. 3b); however, the crystallinity of the obtained CeO_2 was poor. In other words, small CeO_2 particles nucleated into the carbonate precursor framework, subsequently forming aggregated structures. Formation of pores occurred because of the loss of the by-products H_2O and CO_2 (Reaction 6). The formation of the porous structure could also be explained by the large volume change induced owing to the difference in density between $Ce_2(CO_3)_3{\cdot}8H_2O$ (2.790 g/cm^3) and CeO_2 (7.215 g/cm^3) as H_2O_2 diffused into the carbonate. Thus, the original flake-like morphology of $Ce_2(CO_3)_3{\cdot}8H_2O$ could not be maintained during pore formation and stirring during synthesis. Furthermore, the CeO_2 particles had the tendency to aggregate with time to decrease their energy. Hydrothermal treatment destroyed the loose aggregates of CeO_2 derived from the reaction between H_2O_2 and $Ce_2(CO_3)_3{\cdot}8H_2O$. Rearrangement of the CeO_2 particles with good crystallinity *via* a dissolution–recrystallization process occurred under certain temperatures and pressures. Consequently, CeO_2 particles with coarser sizes, smoother surfaces, and mesoporous structures were obtained. Both the mean grain size and pore size increased with increasing hydrothermal times (ESI,† Figure S3). It could be deduced that $Ce_2(CO_3)_3{\cdot}8H_2O$ acted as a template toward the formation of the mesoporous structures. *In situ* CeO_2 nuclei and pores formed simultaneously on the $Ce_2(CO_3)_3{\cdot}8H_2O$ flakes upon addition of H_2O_2. Thus, a large volume change between $Ce_2(CO_3)_3{\cdot}8H_2O$ and CeO_2 instigated formation of the porous structure. The CeO_2 nuclei were surrounded by the pores in the bud though both of the pores and nuclei aggregated and grew subsequently. Moreover, excess NH_4HCO_3 acted as a raising agent to increase/regulate CeO_2 volume by repeatedly producing gases in the mother solution during hydrothermal treatment. Consequently, CeO_2 particles were unable to undergo self-rearrangement into well-crystalline hollow or dense particles, but rather into meso-particles owing to steric effects despite using longer hydrothermal treatments of 36 h at 200 °C.

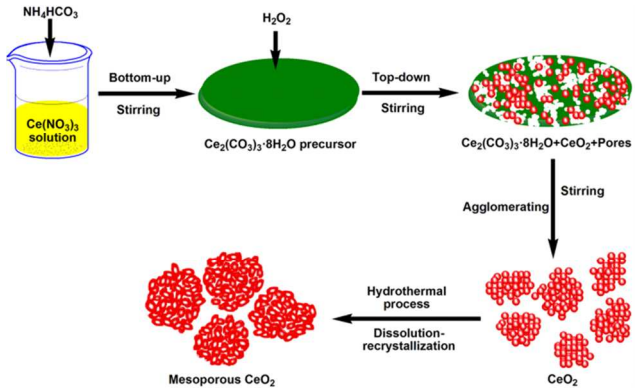

Fig. 6. Illustration of the possible evolution mechanism of mesoporous CeO_2.

Adsorption studies

AO7 and BO2 dyes were selected as model targets to evaluate the adsorption ability of the mesoporous CeO_2 powders in the dark (0−60 min). Figure 7 depicts the effects of different initial concentrations of AO7 and BO2 dyes (20−100 mg/L) on the adsorption efficiency of the mesoporous CeO_2 powders. As observed, the mesoporous CeO_2 powders displayed a stronger adsorption affinity for AO7 over BO2. The adsorption of AO7 may be ascribed to the chelation interaction between the electron-rich groups (sulfonate group, SO_3^-) of AO7 and empty 4*f* orbital of cerium ion on the surface of CeO_2.[42,43] The AO7 adsorption efficiencies achieved within 60 min of reaction were 100, 99.97, 99.97, 98.57, and 90.70 % at initial AO7 concentrations of 20, 40, 60, 80, and 100 mg/L, respectively. Furthermore, it could be observed that the adsorption of AO7 dye was rapid at the early stages of the process at all initial AO7 concentrations studied. In fact, the adsorption process was mostly complete within 10 min of reaction. No significant changes were observed from 20 to 60 min, which indicated that an adsorption–desorption equilibrium between the AO7 molecules and adsorbent was reached within the first 10 min. The rapid and remarkable adsorption efficiency of the mesoporous CeO_2 powders for AO7 is explained as follows. The mesoporous CeO_2 powders possess a high surface area (166.5 m^2/g), which could provide numerous sites for adsorption of the AO7 molecules, thereby increasing the adsorption capacity. The specific surface areas of most CeO_2 powders reported in literature studies are below 100 m^2/g, except for a few studies that report higher surface areas of ~200 m^2/g.[21,44] The pore structure of the mesoporous CeO_2 powders is conducive to transporting the AO7 molecules to the adsorbent framework and increasing the effective contact area between the adsorbent and AO7 molecules.

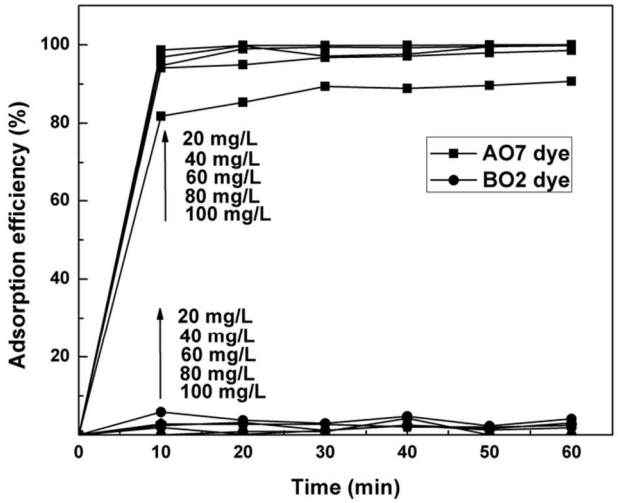

Fig. 7. Time-dependence of adsorption profiles of AO7 and BO2 dyes obtained at varying initial dye concentrations in the dark and presence of mesoporous CeO_2 adsorbent (T = 25 °C; adsorbent dose = 2.0 g/L; in the dark; no pH pre-adjustments).

The effects of the AO7 initial concentration on the AO7 adsorption amount and efficiency in the first 10 min of reaction are shown in Fig. 8. As observed, the adsorption amount increased almost linearly with increasing AO7 initial concentrations. In contrast, the removal efficiency decreased with increasing AO7 initial concentrations. More specifically, when the initial concentration of AO7 was less than 80 mg/L, removal efficiencies greater than 90.0 % were obtained, achieving a maximum value of 98.65 % at [AO7] = 20 mg/L in the first 10 min of reaction.

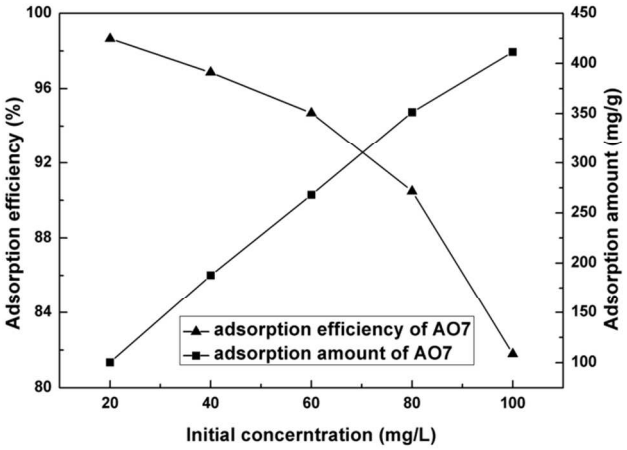

Fig. 8. Effects of AO7 initial concentration on the AO7 adsorption efficiency and adsorption amount in the first 10 min of reaction measured in the dark and presence of mesoporous CeO_2 adsorbent. (T = 25 °C; adsorbent dose = 2.0 g/L; in the dark; no pH pre-adjustments)

The saturated adsorption amount of AO7 was obtained according to the Langmuir linear fitting. The Langmuir linear fit of the experimental data of the adsorption of AO7 dye onto mesoporous CeO_2 is showed in Fig. 9. The corresponding Langmuir parameters obtained at 298 K were as follows: q_m =

510.2 mg/g and K_L = 0.2290. A high associated correlation coefficient R^2 of 0.9925 was obtained, confirming that the Langmuir isotherm model is a good fit for modelling the adsorption of AO7 onto CeO_2 (Table 1).

Table 1. Relevant parameters of Langmuir fitting.

Temperature (K)	Langmuir isotherm model		
	q_m (mg/g)	K_L (L/mg)	R^2
298	510.2	0.2290	0.9925

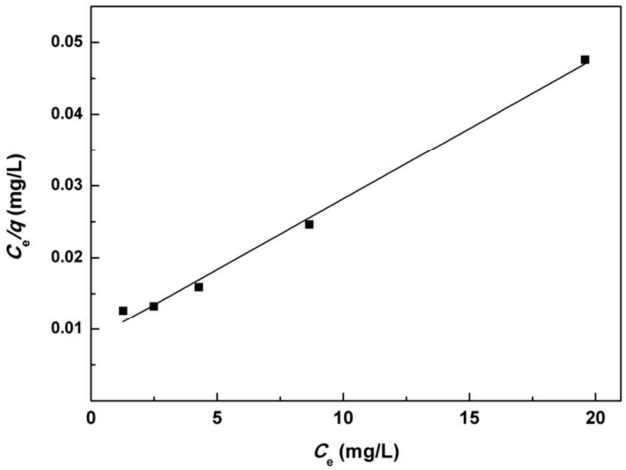

Fig. 9. Langmuir linear fit of AO7 adsorbed onto mesoporous CeO_2 powders.

Conclusions

In this article, mesostructured CeO_2 particles were prepared in the absence of external templates using a combined bottom-up and top-down route. H_2O_2 was introduced as an oxidant to speed up the formation of CeO_2 from $Ce_2(CO_3)_3{\cdot}8H_2O$. A subsequent hydrothermal treatment at 200 °C was employed. Differences in the morphology of the products obtained before and after the hydrothermal treatment were observed. The particles grew larger and featured smoother surfaces and mesoporous structures following hydrothermal treatment. The synthesized mesostructured CeO_2 particles possessed excellent adsorption capacity for AO7 dye compared with BO2 dye. The AO7 adsorption capacity of the mesoporous CeO_2 was determined by fitting the experimental data with the Langmuir model. The saturated adsorption amount was 510.2 mg/g at 298 K. The results revealed that the mesostructured CeO_2 powders can be used as a suitable sorbent for the removal of AO7 dye.

Acknowledgments

The authors appreciate the financial support from the National Science Foundation of China (NSFC51372006); the Scientific Research Starting Foundation for Returned Overseas Chinese Scholars, Ministry of Education; and the Start-Up Fund for High-End Returned Overseas Talents (Renshetinghan 2010, No. 411), Ministry of Human Resources and Social Security, China.

Notes and references

[a] *Key Laboratory of Aerospace Materials and Performance (Ministry of Education), School of Materials Science and Engineering, Beihang University, Beijing 100191, China. Fax: 86-10-8231-6500; Tel: 86-10-8231-6500; E-mail: ruixingli@yahoo.com*

† Electronic Supplementary Information (ESI) available: [details of any supplementary information available should be included here]. See DOI: 10.1039/b000000x/

‡ Footnotes should appear here. These might include comments relevant to but not central to the matter under discussion, limited experimental and spectral data, and crystallographic data.

1 A.V. Soldatov, T.S. Ivanchenko, S. Della Longa, A. Kotani, Y. Iwamoto and A. Bianconi, *Physical Review B*, 1994, **50**, 5074.
2 P. Fornasiero, G. Balducci, R. Di Monte, J. Kašpar, V. Sergo, G. Gubitosa, A. Ferrero and M. Graziani, *J. Catalysis*, 1996, **164**, 173.
3 M. Mogensen, T. Lindegaard, U.R. Hansen and G. Mogensen, *J. Electrochem. Soc.*, 1994, **141**, 2122.
4 Y. Zhang, S. Andersson and M. Muhammed, *Appl. Catal. B-Environ.*, 1995, **6**, 325.
5 H.X. Mai, L.D. Sun, Y.W. Zhang, R. Si, W. Feng, H.P. Zhang, H.C. Liu and C.H. Yan, *J. Phys. Chem. B*, 2005, **109**, 24380.
6 H. Xiao, Z. Ai and L. Zhang, *J. Phys. Chem. C*, 2009, **113**, 16625.
7 H. Li, G. Wang, F. Zhang, Y. Cai, Y. Wang and I. Djerdj, *RSC Adv.*, 2012, **2**, 12413.
8 A. Trovarelli, *Catal. Rev.*, 1996, **38,** 439.
9 R. Li, S. Yabe, M. Yamashita, S. Momose, S. Yoshida, S. Yin and T. Sato, *Solid State Ionics*, 2002, **151**, 235.
10 T. Masui, M. Yamamoto, T. Sakata, H. Mori and G.Y. Adachi, *J. Mater. Chem.*, 2000, **10**, 353.
11 S.H. Lee, Z. Lu, S.V. Babu and E. Matijević, *J. Mater. Res.*, 2002, **17**, 2744.
12 H. Yahiro, Y. Eguchi, K. Eguchi and H. Arai, *J. Appl. Electrochem.*, 1988, **18**, 527.
13 B.D. Gates, Q. Xu, M. Stewart, D. Ryan, C.G. Willson and G.M. Whitesides, *Chem. Rev.*, 2005, **105**, 1171.
14 C.J. Brinker and D.R. Dunphy, *Curr. Opin. Colloid In.*, 2006, **11**, 126.
15 J.Y. Cheng, C. A. Ross, H.I. Smith and E.L. Thomas, *Adv. Mater.*, 2006, **18**, 2505.
16 Y. Wang and Y. Xia, *Nano Letters*, 2004, **4**, 2047.
17 A. Pinna, B. Lasio, M. Piccinini, B. Marmiroli, H. Amenitsch, P. Falcaro, Y. Tokudome, L. Malfatti and P. Innocenzi, *ACS Appl. Mater. Inter.*, 2013, **5**, 3168.
18 I. Medina-Ramirez, M. Gonzalez-Garcia, S. Palakurthi and J. Liu, *Green chemistry-environmentally benign approaches*, 2012, 33.
19 W. Li, Y. Deng, Z. Wu, X. Qian, J. Yang, Y. Wang, D. Gu, F. Zhang, B. Tu and D. Zhao, *J. Am. Chem. Soc.*, 2011, **133**, 15830.
20 C. Ni, X. Li, Z. Chen, H.Y.H. Li, X. Jia, I. Shah and J.Q. Xiao, *Micropor. Mesopor. Mat.*, 2008, **115**, 247.
21 T. Wang, L. Zhang, J. Zhang and G. Hua, *Micropor. Mesopor. Mat.*, 2013, **171**, 196.
22 N. Nabih, R. Schiller, I. Lieberwirth, E. Kockrick, R. Frind, S. Kaskel, C.K. Weiss and K. Landfester, *Nanotechnology*, 2011, **22**, 135606.
23 W. Shi, Y. Li, J. Hou, H. Lv, X. Zhao, P. Fang, F. Zheng and S. Wang, *J. Mater. Chem. A*, 2013, **1**, 728.
24 B. Lu, Z. Li and K. Kawamoto, *Mater. Res. Bull.*, 2013, **48**, 2504.
25 K. Vinodgopal, J. Peller, O. Makogon and P.V. Kamat, *Water Res.*, 1998, **32**, 3646.
26 A. Reife, *Kirk-Othmer encyclopedia of chemical technology*, 1993.
27 K. Tanaka, K. Padermpole and T. Hisanaga, *Water Res.*, 2000, **34**, 327.
28 F. Zhang, C. Feng, W. Li and J. Cui, *Int. J. Electrochem. Sci.*, 2014, **9**, 943.
29 H.H. Bay, C.K. Lim, T.C. Kee, I. Ware, G.F. Chan, S. Shahir and Z. Ibrahim, *Environ. Sci. Pollut. R.*, 2014, **21**, 3891.
30 D. Sun, M. Gu, R. Li, S. Yin, X. Song, B. Zhao, C. Li, J. Li, Z. Feng and T. Sato, *Appl. Surf. Sci.*, 2013, **280**, 693.

31 V. Bekiari and P. Lianos, *Chem. Mater.*, 2006, **18**, 4142.
32 D.J. Alderman, *J. Fish Dis.*, 1985, **8**, 289.
33 M.L. Ma, J.H. Qin, C. Ji, H. Xu, R. Wang, B.J Li, S.Q. Zang, H.W.Hou and S.R. Batten, *J. Mater. Chem. C*, 2014, **2**, 1085.
34 S. Duran, D. Şolpan and O. Güven, *Nucl. Instrum. Meth. B*, 1999, **151**, 196.
35 I. Langmuir, *J. Am. Chem. Soc.*, 1918, **40**, 1361.
36 K.R. Hall, L.C. Eagleton, A. Acrivos and T. Vermeulen, *Ind. Eng. Chem. Fund.*, 1996, **5**, 212.
37 Y. Hayashi, S. Hosokawa, S. Imamura and M. Inoue, *J. Ceram. Soc. JPN*, 2007, **115**, 592.
38 S. Liu, R. Ma, R. Jiang and F. Luo, *J. Cryst. Growth*, 1999, **206**, 88.
39 J.C. Groen, L.A. Peffer and J. Pérez-Ramírez, *Micropor. Mesopor. Mat.*, 2003, **60**, 1.
40 T. Wang, O. Sel, I. Djerdj and B. Smarsly, *Colloid Polym. Sci*., 2006, **285**. 1.
41 J. G. Li, T. Ikegami, Y. Wang and T. Mori, *J. Am. Ceram. Soc.*, 2003, **86**, 915.
42 P. Ji, J. Zhang, F. Chen and M. Anpo, *Appl. Catal. B*, 2009, **85**, 148.
43 C. Guillard, H. Lachheb, A. Houas, M. Ksibi, E. Elaloui and J.M. Herrmann, *J. Photoch. Photobio. A*, 2003, **158**, 27.
44 S.C. Laha and R. Ryoo, *Chem. Commun.*, 2003, **17**, 2138.